Three-Dimensional End-to-End Modeling and Analysis for Graphene-Enabled Terahertz Band Communications

Chong Han, *Member, IEEE,* and Ian F. Akyildiz, *Fellow, IEEE*

***Abstract*—Terahertz (0.1-10 THz) band communication is envisioned as a key technology to satisfy the increasing demand for ultra-high-speed wireless links. In this paper, a three dimensional (3-D) end-to-end model in the THz band is developed, which includes the graphene-based reflectarray antenna response and the 3-D multi-path propagation phenomena. In particular, the architecture of a graphene-based reflectarray antenna is investigated and the 3-D radiation pattern is modeled. Moreover, a 3-D THz channel model based on ray tracing techniques is developed, as a superposition of the line-of-sight (LoS), reflected and scattered paths. By using the developed end-to-end model, an in-depth analysis on the 3-D channel characteristics is carried out. Specifically, the gain at the main beam of the graphene-based reflectarray antenna is 18 dB, and the 3-dB beamwidths in the elevation and azimuth planes are 7^o and 10^o respectively. The use of the reflectarray leads to a decrease of the delay spread from 1.23 ns to 0.099 ns, which suggests that the resulting coherence bandwidth reaches 2 GHz. Moreover, the rms angular spread in the elevation plane is less than 0.12^o, which is 1/10 of that without beamforming. Furthermore, the wideband channel capacity at THz frequencies is characterized, which can be enhanced with a larger transmit power, a lower operating frequency, a larger bandwidth and a higher beamforming gain. Finally, the beamforming gain enabled by the reflectarray antenna is compromised at the cost of the strict beam alignment, and the deviation needs to be smaller than 11^o. The provided analysis and the channel physical parameters lay out the foundation and are particular useful for realizing reliable and efficient ultra-high-speed wireless communications in the THz band.**

***Index Terms*—Terahertz Band, 3-D channel, Graphene, Reflectarray Antenna, Wideband.**

I. Introduction

In recent years, the wireless data traffic grew exponentially, further accompanied by an increasing demand for higher data rates. The data rates have doubled every eighteen months over the last three decades and are currently approaching the capacity of wireless systems [1]. Following this trend, wireless data rates of 100 Gbps and even 1 Tbps will become reality within the next decade [2]. In addition to many proposed solutions for next generation advanced cellular systems, the Terahertz band, i.e., 0.1-10 THz, is considered as one of the most promising spectrum bands to support ultra-high-speed wireless communications in the future [3]. With its ability to offer an ultra-broad bandwidth and very high data rates, the use of the THz band is envisioned to address the spectrum scarcity and capacity limitations of current wireless systems, and boost a plethora of applications, including ultra-high-speed wireless backhaul to the small cells, and ultra-high-speed data transfers among proximal devices [4]. Furthermore, related to vehicular networks, THz band communications [5] can be applied in intelligent transport systems for intra-vehicle, inter-vehicle and vehicle-to-roadside wireless ultra-broadband links.

For the realization of efficient wireless communication networks in the THz band, it is imperative to develop an accurate three-dimensional (3-D) channel model which accurately characterizes the Terahertz spectrum peculiarities in both the elevation and azimuth planes. In realistic application scenarios, the multi-path rays arrive at the receiver from both the azimuth and elevation planes, which is the result of the 3-D radiation diagram of the antennas and the 3-D propagation of the electromagnetic waves in the channel. These facts introduce an angular spread in the elevation plane, and influence the channel physical peculiarities. The first model that recognizes the elevation coordinate in a 3-D model was proposed in [6], in which the author assumed the arriving signals were uniformly distributed in the azimuth plane and non-uniformly distributed in the elevation plane. Further development provides analytical solutions of the power spectral density of the received signal in the three dimensions and produces the desired spatio-temporal characteristics of 3-D wireless channels as studied in [7], [8]. However, these models for lower frequency bands do not capture the behavior of the THz band, such as the very high molecular absorption loss or the very high reflection loss. Existing THz band channel models in [9], [10], [11], [12] are developed for 2-D cases, which fail to describe signal variations in the elevation plane. Furthermore, THz antenna responses are not included in these models. Consequently, there is a need for an end-to-end model, which captures the antenna response and the 3-D multi-path propagation, and investigates the resulting channel characteristics.

Graphene-based antennas to operate in the THz band are suggested in [13], [14], [15], due to the fact that graphene supports the propagation of surface plasmon polariton (SPP) waves. The main merit of using graphene-based antennas is that the equivalent electrical size is much larger than its physical dimensions, owing to the much lower speed of SPP waves in a graphene-based antenna compared to that of free-space electromagnetic waves in a metallic antenna [15]. To overcome the very high path loss at THz frequencies, reflectarray antenna technologies [16] are very attractive among others. In partic-

This work was supported by the U.S. National Science Foundation (NSF) under Grant No. ECCS-1608579 and in part by Alexander von Humboldt Foundation through Dr. Ian F. Akyildiz's Humboldt Research Prize in Germany.

Chong Han is with the University of Michigan–Shanghai Jiao Tong University Joint Institute, Shanghai Jiao Tong University, Shanghai 200240, China. (e-mail:chong.han@sjtu.edu.cn).

Ian F. Akyildiz is with the Broadband Wireless Networking Laboratory (BWN-Lab), School of Electrical and Computer Engineering, Georgia Institute of Technology, Atlanta, GA 30332, USA (e-mail: ian@ece.gatech.edu).

ular, the reflectarray antenna technologies take the advantage of parabolic reflectors and phased arrays. This approach is especially beneficial in providing high directivity gain with low losses at high frequencies, e.g., the THz band. In the literature, the reflectarray antennas are studied in microwave and millimeter-wave bands [17]. More recently, these techniques are experimentally demonstrated [18] and theoretically analyzed at THz frequencies [19], [20], from the antenna design perspective. However, the integration of the graphene-based reflectarray antenna response into the THz band channel model, and the influences on the channel peculiarities have not been characterized from the communication perspective [21].

In this paper, we develop a unified 3-D end-to-end model in the THz band, by capturing the response of the graphene-based reflectarray antenna and the 3-D multi-path propagation phenomena. Using the developed model, we present an in-depth analysis on the 3-D channel characteristics and the influence of directivity from graphene-based reflectarray antennas in the THz band. Compared with our prior work in [22], this paper provides the detailed mathematical derivations for the graphene-based reflectarray antenna response and includes more detailed, extensive 3-D channel characterization. The distinctive contributions of this work are summarized as follows.

- **We develop an analytical 3-D end-to-end model in the THz band, which includes the responses of the graphene-based reflectarray antenna and the 3-D multi-path propagation channel.** In particular, the architecture of a graphene-based reflectarray antenna is investigated and the 3-D radiation pattern is modeled. Moreover, a 3-D THz channel model is developed based on ray tracing techniques, as a superposition of the line-of-sight (LoS), reflected and scattered paths.
- **We present an in-depth analysis on the 3-D channel characteristics and the influence of directivity from graphene-based reflectarray antennas in the THz band.** In particular, we thoroughly characterize the antenna gain and the beamwidth, the delay spread and the coherence bandwidth, the 3-D angular spread, the wideband channel capacity, and the beam misalignment influence.

The provided analysis and the channel physical parameters lay out the foundation and are particularly useful for the physical and upper layers design for reliable and efficient ultra-high-speed wireless communications in the THz band. The rest of the paper is organized as follows. In Sec. II, a 3-D end-to-end channel model in the THz band is developed. Then, the graphene-based reflectarray antenna is investigated and the radiation pattern is modeled in Sec. III. Moreover, the 3-D multi-path channel model in the THz band that consists of the LoS, reflected and scattered rays is analyzed in Sec. IV. Using the developed model, we present an in-depth analysis on the 3-D channel characteristics in Sec. V. Finally, the paper is concluded in Sec. VI.

II. A 3-D End-To-End Model in the Terahertz Band

In this section, we develop an end-to-end model, which includes frequency response in a 3-D environment from the transmitting to the receiving antenna in the (0.1-10) THz band. Since the wave propagation in the THz band is frequency-dependent, the model is developed as a combination of a number of sub-bands, which are narrow enough to be considered as flat fading channels. The operating frequency, f, takes values from $\{f_1, f_2 \ldots, f_n, \ldots\}$, where f_n is the center frequency of the n^{th} sub-band. The bandwidth of each sub-band is identical and equal to $\Delta f = f_{n+1} - f_n$.

In the end-to-end channel model, the transfer function $H_{\text{e2e}}(f)$ of the end-to-end response can be expressed as a sum of the transfer function of all arrival rays,

$$H_{\text{e2e}}(f) = \sum_{i=1}^{I} A_T^{(i)}(f) H^{(i)}(f) A_R^{(i)}(f), \tag{1}$$

where $A_T^{(i)}$ and $A_R^{(i)}$ denote the frequency responses of the transmitting and the receiving antennas for the i^{th} ray. Moreover, $H^{(i)}$ describes the frequency response of i^{th} ray propagating in the THz channel. I is the total number of multi-path components in a 3-D environment. Even with antenna directivity, the antenna radiation pattern has 3-D beamwidth, which results that the multi-path effect still exists but is confined in the radiation sector [23]. Indeed, the number of multi-path components decreases with the reducing antenna beamwidth. Next, we describe the mathematical models to capture the graphene-based reflectarray antenna response and characterize the 3-D multi-path channel in the THz band.

III. Graphene-based Reflectarray Antenna Response

The main constraint of THz band communications is imposed by the very high and frequency-selective path loss, which can easily above 100 dB for distances over 1m [9]. One promising approach to enhance the received power is to provide directivity gain by using reflectarray antenna technologies, which has been experimentally demonstrated [18] and theoretically analyzed at THz frequencies [19], [20]. By reflecting the incident waves from a THz source, the far-field radiation pattern can be collimated and created as a pencil-sharp beam in a desired direction, as illustrated in Fig. 1.

In this architecture, the reflectarray consists of an array of graphene reflective cells, which introduce appropriate phase-shift from reflection of the incident THz waves. The resulting radiation from the far-field becomes a pencil-sharp beam. This design combines the features of parabolic reflectors and conventional phased arrays with low losses, compact profile and high efficiency. In the following of this section, the complex conductivity of graphene, the complex wave vector and ultimately, the radiation pattern of reflectarray antenna are investigated.

A. Complex Conductivity of Graphene

Graphene can be modeled as an infinitely thin surface with complex conductivity due to its mono-atomic thickness. Then, the conductivity σ_g is given as a sum of the intraband σ_{intra} and interband σ_{inter} contributions according to Kubo's formula [24], [25],

$$\sigma_g(f) = \sigma_{\text{intra}}(f) + \sigma_{\text{inter}}(f), \tag{2}$$

where

$$\sigma_{\text{intra}}(f) = \frac{jq_e^2}{\pi\hbar^2(2\pi f + j/\tau)} \cdot \int_0^\infty n_F(\epsilon - E_F) - n_F(\epsilon + E_F)d\epsilon, \quad (3)$$

$$\sigma_{\text{inter}}(f) = j2q_e^2 f \int_0^\infty \frac{n_F(\epsilon - E_F) - n_F(-\epsilon - E_F)}{(2\epsilon)^2 - (2\pi f\hbar + j/2\tau)}d\epsilon. \quad (4)$$

In the above equations, q_e is the electron charge, $\hbar$ refers to the reduced Planck constant, E_F is the Fermi level, n_F denotes the Fermi-Dirac distribution function, and τ is the momentum relaxation time due to the carrier intraband scattering. By considering only the intraband contribution and completing the intergral in (3), an approximation to (2) is given by

$$\sigma_g(f) \approx -\frac{jq_e^2 k_B T}{\pi\hbar^2(2\pi f - j/\tau)}\left(\frac{\mu_c}{k_B T} + 2\ln\left(\mathrm{e}^{-\mu_c/k_B T} + 1\right)\right), \quad (5)$$

where k_B represents the Boltzmann constant, T is the temperature, and μ_c denotes the chemical potential.

B. Complex Wave Vector of Graphene

The complex wave vector of SPP waves in graphene determines the propagation properties of SPP waves, and is dependent on the conductivity in (5). The dispersion equation that relates the complex wave vector k_{spp}, the complex conductivity σ_g, and the permittivity ϵ_r of the surrounding materials of graphene patches, is described as

$$\frac{\epsilon_{r1}}{\sqrt{k_{\text{spp}} - \epsilon_{r1}k_0^2}} + \frac{\epsilon_{r2}}{\sqrt{k_{\text{spp}} - \epsilon_{r2}k_0^2}} = -\frac{j\sigma_g}{2\pi f\epsilon_0}, \quad (6)$$

where ϵ_{r1} and ϵ_{r2} denote the permittivity values of the materials above and below graphene patches, respectively. Moreover, ϵ_0 refers to the vacuum permittivity, and $k_0 = 2\pi f/c$ is the free space wavenumber where c is the speed of light.

As shown in Fig. 1, the graphene patch is a rectangular nano-strip and has a finite length l and width w. Since the SPP mode can propagate on finite width nano-strips, a condition on the nano-strip length that results from the complex wave vector in (6) to support standing wave resonances is

$$l = \alpha\frac{\lambda_{\text{spp}}}{2} = \alpha\frac{\pi}{\text{Re}\{k_{\text{spp}}\}}, \quad (7)$$

where $\lambda_{\text{spp}} = 2\pi/\text{Re}\{k_{\text{spp}}\}$ stands for the SPP wavelength, and α is an integer SPP mode number.

C. Radiation Pattern of Reflectarray Antenna

In Fig. 1, the THz source is assumed to have a phase center located at the origin of the 3-D axes. The $(m,n)^{\text{th}}$ cell of the reflectarray scatters the incoming ray from the source to a desired direction, by applying a phase correction. By denoting $\vec{p}_{mn}$ as the position vector of the incoming ray from the source, and $\hat{p}_o$ as the desired direction of the pencil-sharp beam, the phase of the reflectarray needs to satisfy

$$k_0(\vec{p}_{mn} - \vec{P}_{mn} \cdot \hat{p}_o) - \psi_{mn} = 2\pi\beta, \quad (8)$$

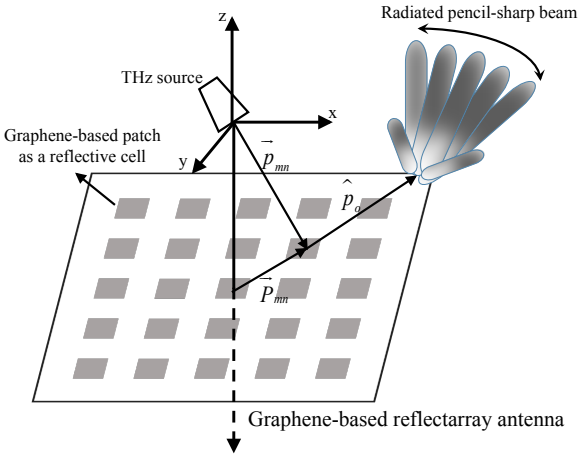

Fig. 1. An architecture of graphene-based reflectarray antenna.

where $\vec{P}_{mn}$ is a position vector of the $(m,n)^{\text{th}}$ cell, and $\beta \geqslant 0$ is an integer. A phase shift ψ_{mn} is introduced between the incident and scattered field from the $(m,n)^{\text{th}}$ reflectarray cell, to allow that the phase of the scattered field from the entire reflectarray is uniform in a plane normal to the direction of the desired beam $\hat{p}_o$. This results in that the reflectarray collimates the waves from the THz source into a pencil-sharp beam in the far-field.

Based on the proposed architecture in Fig. 1, the far-field radiation gain of the reflectarray in the direction (θ,ϕ) at the frequency f can be obtained as

$$A_T(f) = \eta_{\text{s}}G_g(f,\theta,\phi)\cos(\theta) \cdot \sum_{n=0}^{N-1}\sum_{m=0}^{M-1} R_{mn}(f,\theta_{mn},\phi_{mn},\psi_{mn}) \cdot \exp\left(jk_0\left[x'_{mn}\sin(\theta)\cos(\phi) + y'_{mn}\sin(\theta)\sin(\phi)\right] + j\psi_{mn}\right), \quad (9)$$

where M, N are the number of cells in the x-axis and y-axis of the reflectarray, η_{s} is the radiation efficiency of the THz source, and G_g describes the gain of the individual nano-strip graphene-based patch.

Importantly, R_{mn} denotes the magnitude of the reflection coefficient of the $(m,n)^{\text{th}}$ cell of the graphene reflectarray, which depends on the graphene conductivity as obtained in (5), the wave vector of SPP waves in graphene as computed in (6), the nano-strip length as provided in (7), and the phase correction as analyzed in (8).

On the other hand, the frequency response of the graphene antenna at the receiver is computed as:

$$A_R(f) = \sqrt{e_R(f)D_R(f,\theta,\phi)\frac{\lambda^2}{4\pi}}, \quad (10)$$

where e_R is the receiver antenna radiation efficiency. D_R is the directivity of the receiving antenna, which is a function of frequency, the elevation and the azimuth angles of arrival. Here we assume an omni-directional receiving antenna, in which the radiation efficiency is unitary and the directivity is uniform in the elevation and azimuth planes. Then, the aperture of the receiving antenna $\frac{\lambda^2}{4\pi}$ is included. Hence, the impact of the

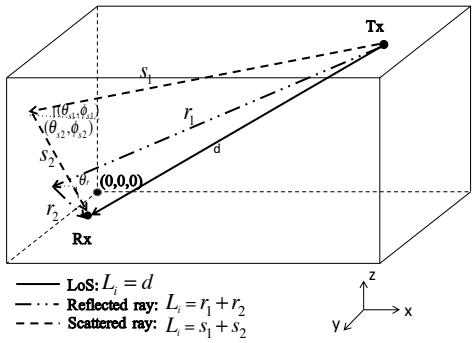

Fig. 2. A 3-D geometry of THz propagation model between the transmitter (Tx) and the receiver (Rx).

graphene-based reflectarray antenna at the transmitter on the 3-D channel response is investigated as a focus.

IV. 3-D Channel Model in the Terahertz Band

In this section, we develop a 3-D THz channel model based on ray tracing techniques, as a superposition of the LoS, reflected and scattered paths. The ray tracing techniques have been proved to enable very good prediction capabilities at Terahertz frequencies [10]. The diffraction path can be ignored in general since it contributes negligibly to the received signal power. The only exception is when the receiver is in the very closed region near the incident shadow boundary [26], which is not considered in this work. The geometry configuration is demonstrated in Fig. 2, where the traveling distance of the i^{th} ray is given by

$$L_i = \begin{cases} d & \text{LoS} \\ r_1 + r_2 & \text{Reflected Rays} \\ s_1 + s_2 & \text{Scattered Rays} \end{cases} \tag{11}$$

where d is the direct distance between the transmitter and the receiver. For reflection, r_1 is the distance from the transmitter to the reflecting point, and r_2 is the distance from the reflecting point to the receiver. For scattering, s_1 is the distance from the transmitter to the scattering point, and s_2 is the distance from the scattering point to the receiver.

The channel transfer function for the i^{th} ray $H^{(i)}$ in (1) is given in (12) on the next page. In this equation, $\tau_i = L_i/c$ is the time-of-arrival of the ray and c denotes the speed of light. In the LoS model, k_{ma} is the frequency-dependent medium absorption coefficient, which depends on the composition of the transmission medium and is detailed in [9]. Furthermore, the spreading loss of $\sqrt{1/(4\pi d^2)}$ is accounted for, while the aperture has already been included in (10).

In the reflected ray model, the Fresnel reflection coefficient for the transverse magnetic (TM) polarized waves γ_{TM} on a smooth surface, which is consistent with the SPP mode on the graphene-based reflectarray according to (6), is computed as

$$\gamma_{\text{TM}}(f) = \frac{\sqrt{1 - \left(\frac{1}{n_t}\sin(\theta_{\text{r}})\right)^2} - n_t \cos(\theta_{\text{r}})}{\sqrt{1 - \left(\frac{1}{n_t}\sin(\theta_{\text{r}})\right)^2} + n_t \cos(\theta_{\text{r}})}$$

$$\approx \exp\left(\frac{-2n_t \cos(\theta_{\text{r}})}{\sqrt{1 - \frac{1}{n_t^2}}}\right), \tag{13}$$

where θ_{r} is the angle of incident wave and can be computed using the law of cosine, i.e., $\theta_r = \frac{1}{2}\cos^{-1}\left(\frac{r_1^2 + r_2^2 - d^2}{2r_1 r_2}\right)$. In addition, n_t refers to the refractive index, varying with the frequencies and reflecting material. As we consider the reflected rays with large incident angles, the Taylor's approximation for the smooth surface reflection coefficient in (13) shows good accuracy at Terahertz frequencies.

In order to characterize the effect of the surface roughness, a Rayleigh factor is introduced as

$$\rho(f) = \exp\left(-\frac{8\pi^2 \cdot f^2 \cdot \sigma_{\text{rough}}^2 \cdot \cos^2(\theta_{\text{r}})}{c^2}\right), \tag{14}$$

where σ_{rough} is the rough surface height standard deviation.

In the scattered ray model, the scattering geometry is considered on the tangent plane (the incident azimuth angle ϕ_{s1} is π), and θ_{s1} stands for the elevation angle of the incident wave. In addition, θ_{s2} and ϕ_{s2} denote the elevation and azimuth angles of the scattered wave, respectively. The scattering coefficient $S(f)$ of rough surfaces according to the modified Beckmann-Kirchhoff theory [10] is given by

$$S(f) \approx \exp\left(\frac{-2n_t \cos(\theta_{s1})}{\sqrt{1 - \frac{1}{n_t^2}}}\right) \cdot \sqrt{\frac{1}{1 + g + \frac{g^2}{2} + \frac{g^3}{6}}} \cdot \sqrt{\rho_0^2 + \frac{\pi \cos(\theta_{s1})}{100}\left(g\mathrm{e}^{-v_s} + \frac{g^2}{4}\mathrm{e}^{-v_s/2}\right)} \tag{15}$$

The parameters in this model are

$$g = k_0^2 \sigma^2 \left(\cos(\theta_{s1}) + \cos(\theta_{s2})\right)^2, \tag{16}$$

$$\rho_0 = \text{sinc}(v_x l_x) \cdot \text{sinc}(v_y l_y), \tag{17}$$

$$l_x = l_y = 10 l_c, \tag{18}$$

$$v_x = k_0 \cdot \left(\sin(\theta_{s1}) - \sin(\theta_{s2})\cos(\phi_{s2})\right), \tag{19}$$

$$v_y = k_0 \cdot \left(-\sin(\theta_{s2})\sin(\phi_{s2})\right), \tag{20}$$

$$v_s = (v_x^2 + v_y^2) l_c^2 / 4, \tag{21}$$

where $k_0 = 2\pi f/c$ represents the free space wave number, and l_c is the correlation length of the rough surface, and the geometrical factor $F^2 = \cos(\theta_{s1})$ is suitable for large incidence and scattering angles. In the above derivations, we used Taylor's approximation to simplify the expression for the scattering coefficient.

The theoretical 3-D end-to-end model in (1) consists of the graphene reflectarray antenna response and the 3-D multi-path propagation phenomena. In particular, the multi-path propagation model in the THz band in (12) was partially validated in [10].

V. 3-D Channel Characterization

Using the developed propagation model, we present a detailed analysis of the 3-D end-to-end channel characteristics in the THz Band. In particular, we thoroughly characterize the reflectarray antenna gain and the beamwidth, the delay

This article has been accepted for publication in a future issue of this journal, but has not been fully edited. Content may change prior to final publication. Citation information: DOI 10.1109/TVT.2016.2614335, IEEE Transactions on Vehicular Technology

$$H^{(i)}(f) = \begin{cases} \left| \frac{1}{\sqrt{4\pi d^2}} \mathrm{e}^{-\frac{1}{2}k_{\mathrm{ma}}(f)d} \right| \cdot \exp\left(-j2\pi f \tau_i\right) & \text{LoS} \\ \left| \left(\frac{1}{\sqrt{4\pi (r_1+r_2)^2}} \right) \mathrm{e}^{-\frac{1}{2}k_{\mathrm{ma}}(f)(r_1+r_2)} \cdot \gamma_{\mathrm{TM}}(f) \cdot \rho(f) \right| \cdot \mathrm{e}^{-j2\pi f \tau_i} & \text{Reflected Rays} \\ \left| \left(\frac{1}{\sqrt{4\pi (s_1+s_2)^2}} \right) \mathrm{e}^{-\frac{1}{2}k_{\mathrm{ma}}(f)(s_1+s_2)} \cdot S(f) \right| \cdot \mathrm{e}^{-j2\pi f \tau_i} & \text{Scattered Rays} \end{cases} \quad (12)$$

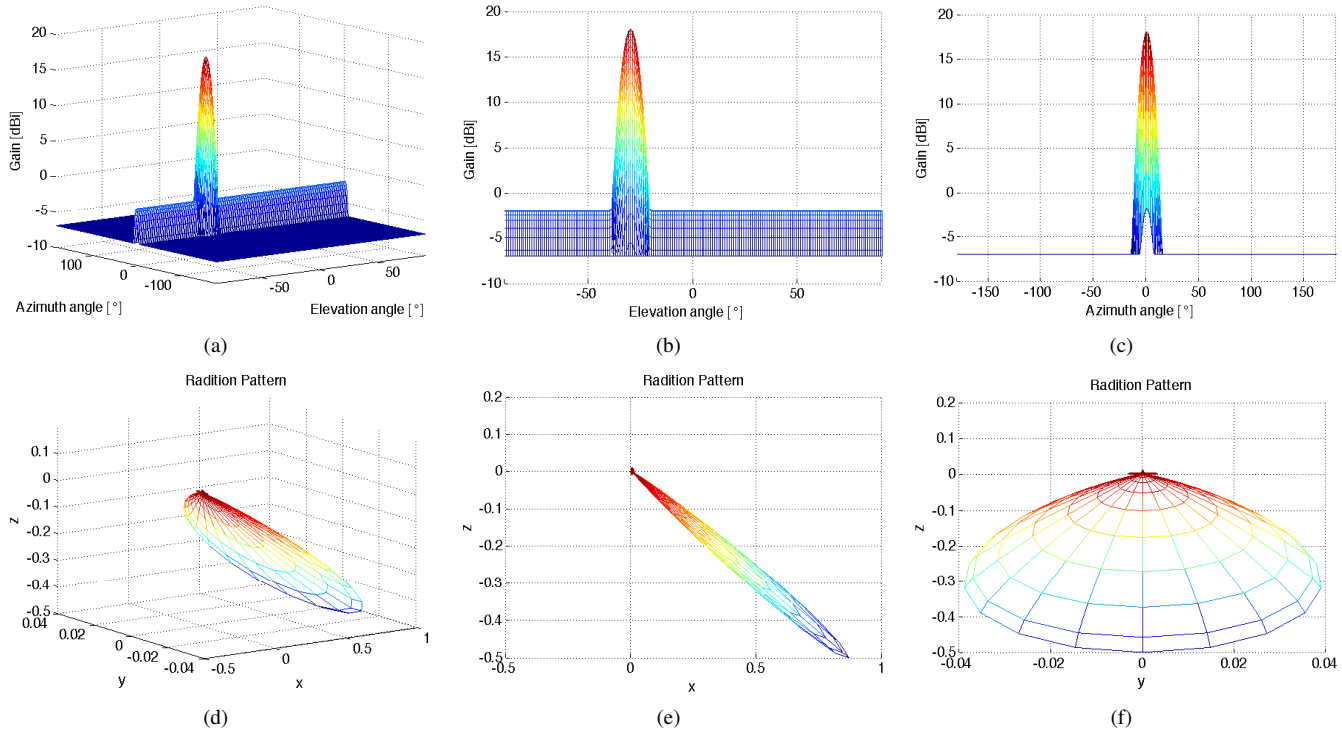

Fig. 3. Gain of a graphene-based reflectarray antenna in 3-D. (a) Gain in 3-D spherical view. (b) Gain in the elevation plane. (c) Gain in the azimuth plane. (d) Radiation Pattern in 3-D cartesian view. (e) Radiation Pattern in the x-z plane. (f) Radiation Pattern in the y-z plane.

spread and the coherence bandwidth, the 3-D angular spread, the channel capacity, and the beam misalignment effect.

Simulation Setup: The simulation is conducted by considering a indoor environment of dimensions $5\mathrm{m}\times\ 4\mathrm{m}\times\ 3\mathrm{m}$, such as a passenger car as shown in Fig. 2. The transmitter (Tx) is located at $(4.8\mathrm{m}, 2\mathrm{m}, 2.9\mathrm{m})$, and the receiver (Rx) is located at $(0.1\mathrm{m}, 2\mathrm{m}, 1\mathrm{m})$. At the transmitter, a graphene-based reflectarray antenna is deployed to provide the directivity gain. On the contrary, an omni-directional antenna is considered at the receiver. Multi-path components in the 3-D environment are captured at the receiver, in which the LoS, the once-reflected, the twice-reflected and the scattered rays are included. The walls are covered by plaster, where its refractive index can be found in [27], while the interactions with the ceiling and the ground are neglected. In the simulations, the main beam of the reflectarray antenna points at the LoS direction.

A. Reflectarray Antenna Gain and Beamwidth

Based on the expression in (9), the far-field gain of the graphene-based reflectarray antenna is numerically evaluated in the spherical coordinates, as illustrated in Fig. 3(a). The maximum gain is 18 dBi in the main lobe, at the frequency of 1 THz. By contrast, the side lobes stay more than 25 dB below the main beam and hence, are neglected in the figures. The 3-dB beamwidths in the elevation and azimuth planes are 7^{o} and 10^{o} respectively, as shown in Fig. 3(b) and Fig. 3(c). The higher gain from the graphene-based reflectarray antenna would appear with the reduction of the beamwidths. The relationship between the antenna gain and the beamwidth depends on the operating frequency, the size of the reflectarray and the spacing, which needs to be rigorously analyzed based on the experimental measurements [19]. Converting to the cartesian coordinates, the far-field radiation pattern is plotted in Fig. 3(d). In particular, a downtilt angle of 30^{o} can be observed from the radiation pattern in the x-z plane (see Fig. 3(e)), which is consistent with the results in Fig. 3(b). On the other hand, a uniform radiation pattern can be found in the y-z plane in Fig. 3(f).

Note that the direction of the main beam can be directed adaptively, by varying the incident angle from the THz source as seen in Fig. 1, or tuning the phase shifts of the reflectarray according to (8). On the one hand, the incident angle has very small impact on the reflection coefficient in graphene-based cells, i.e., less than 1 dB difference according to [19]. Hence,

This article has been accepted for publication in a future issue of this journal, but has not been fully edited. Content may change prior to final publication. Citation information: DOI 10.1109/TVT.2016.2614335, IEEE Transactions on Vehicular Technology

TABLE I
POWER DELAY PROFILE IN THE 3-D CHANNEL AT $f = 1$ THZ

		Reflectarray Tx antenna	Omni-directional Tx antenna
	Time of Arrival [ns]	Path Gain [dB]	Path Gain [dB]
LoS	16.91	-91.66	-109.66
Reflected Ray 1	17.53	-111.57	-129.57
Reflected Ray 2	18.15	-137.13	-130.13
Reflected Ray 3	21.54	-130.47	-123.47
Reflected Ray 4	21.54	-130.47	-123.47
Twice Reflected Ray 1	18.78	-157.43	-150.43
Scattered Ray 1	17.87	-125.13	-140.13
Scattered Ray 2	18.49	-163.79	-156.79
Scattered Ray 3	21.87	-147.88	-140.88
Scattered Ray 4	21.88	-166.01	-159.01
Total Path Gain [dB]		-91.62	-109.23
Average Delay [ns]		19.46	19.46
RMS Delay Spread [ns]		0.099	1.23
Coherent Bandwidth [GHz]		2.0	0.16

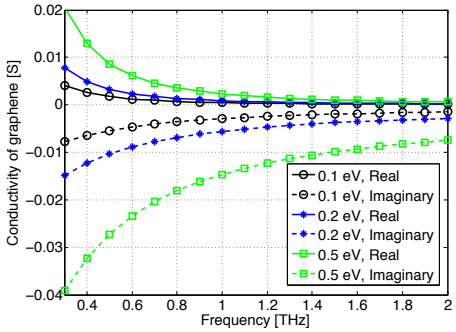

Fig. 4. Complexity conductivity of graphene, for a varying chemical potential.

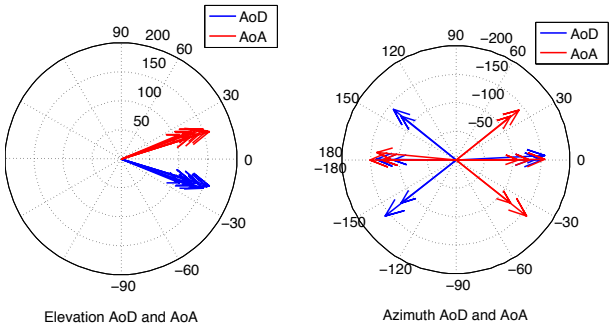

(a) (b)

Fig. 5. Power angle profiles (PAP) for AoD and AoA. (a) Elevation PAP. (b) Azimuth PAP.

the variation of the incident angle influences the radiation direction while has no considerable changes in the shape of the main beam. On the other hand, the graphene-based reflectarray offers the possibility to control the phase of the reflected field at the individual cell level and hence, dynamically reconfigure the far-field radiation pattern [28]. This is achieved by tuning the complex conductivity of graphene through chemical potential variations. For example, as the chemical potential increases from 0.1 eV, 0.2 eV, to 0.5 eV, the absolute values of the real and imaginary parts of the graphene conductivity rise, as shown in Fig. 4. In addition, the conductivity decreases with an increasing frequency.

B. Delay Spread and Coherence Bandwidth

Based on the geometry in Fig. 2, the power delay profile with the graphene-based reflectarray antenna is summarized in Table I. To compare, we also include the results by considering an omni-directional antenna at the transmitter. At the receiver, the LoS, the once-reflected, the twice-reflected and the scattered rays are captured with different delays and gains. The main channel physical parameters such as the total power gain, the average delay, the rms delay spread and the coherence bandwidth are calculated for the two different cases.

The observations from Table I are summarized as follows. The total power gain increases from -109.23 dB to -91.62 dB when the reflectarray antenna is used, and the gain enhancement matches with the gain of the reflectarray antenna as analyzed in Sec. V-A. In addition, the rms delay spread can be obtained as

$$\sigma_{delay} = \sqrt{\overline{\tau^2} - (\overline{\tau})^2}, \tag{22}$$

$$\overline{\tau^x} = \frac{\sum_{i=1}^{I} |\alpha_i|^2 |\tau_i|^x}{\sum_{i=1}^{I} |\alpha_i|^2}, \tag{23}$$

where $\overline{\tau^x}$ describes the first (x=1) or second (x=2) moment of the instantaneous power-delay profile. α_i is the path gain amplitude of the i^{th} path, as $\alpha_i = |A_T^{(i)}(f) H^{(i)}(f) A_R^{(i)}(f)|$ according to (1).

The reflectarray antenna confines the radiation pattern, which results that the number of significant multi-path components decreases. Consequently, the rms delay spread reduces from 1.23 ns to 99 ps. The coherence bandwidth, which is computed as $0.2/\sigma_{delay}$, reaches 2 GHz when the reflectarray antenna is used, which is 12.5 times as large as that in the omnidirectional antenna case. This indicates a large range of frequencies over which the channel can be considered as flat.

We realize that these values of the coherence bandwidth are smaller than the results in the our prior multi-path channel model in [10]. This is due to the variation of the simulation environment and the inclusion of the 3-D components that introduces a additional delay spread from the elevation plane. Furthermore, if we exclude the twice-reflected and scattered rays, the rms delay spread drops slightly to 97 ps (i.e., only 2% difference). Therefore, if we only consider the LoS

This article has been accepted for publication in a future issue of this journal, but has not been fully edited. Content may change prior to final publication. Citation information: DOI 10.1109/TVT.2016.2614335, IEEE Transactions on Vehicular Technology

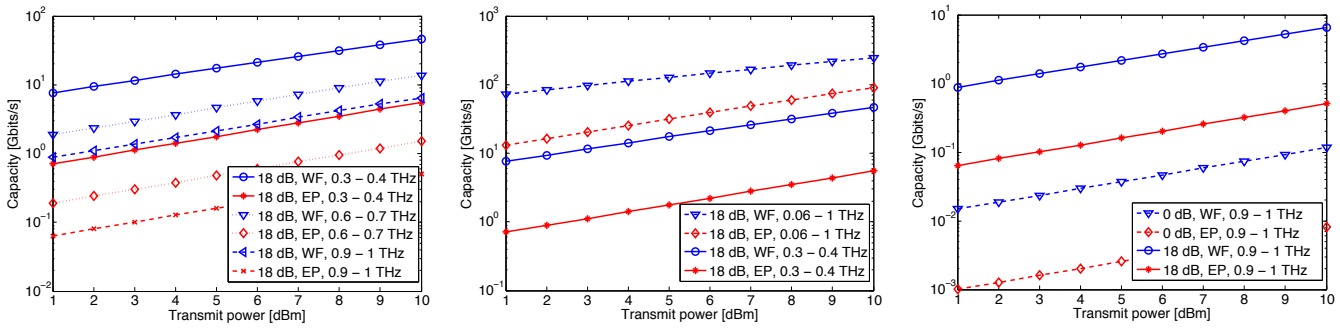

(a) (b) (c)

Fig. 6. Wideband capacity for 3-D channels at $d = 5$m, for the varying transmit power and the water-filling (WF) and equal-power (EP) allocation schemes. (a) Capacity over the three frequency bands, namely, 0.3-0.4 THz, 0.8-0.9 THz and 1.9-2.0 THz. (b) Capacity over the entire 0.06-1 THz band versus 0.3-0.4 THz. (c) Capacity with the 18 dB reflectarray gain versus the omni-directional antenna.

and the reflected paths, the channel characteristic results are sufficiently accurate, since these two propagation types play the dominant roles compared with the other NLoS effects.

C. 3-D Angular Spread

The angular spread is an important factor to evaluate the spatial characteristics of the 3-D channel. To evaluate this, the power angle profiles (PAP) for the elevation angle-of-departure (AoD) and angle-of-arrival (AoA) are demonstrated in Fig. 5(a). The LoS, single-reflected, twice reflected, and scattered rays are all taken into account. In particular, the zero degree lies in the x-y plane, and the degree increases as pointing upwards in the positive z-axis. This suggests the range of the elevation angles is between -90^{o} and 90^{o}. Since the Tx is located near the ceiling pointing downwards (see Fig. 2), the elevation AoDs are below zero degrees.

The AoAs are coupled with the AoDs. In the elevation plane, since the height of the transmitter is much larger than the receiver (see Fig. 2), the elevation AoAs are reciprocal to the elevation AoD and are greater than zero degrees. In the azimuth plane, the relationship between the AoAs and the AoDs is categorized according to the specific geometry. First, for the LoS path, the AoA and the AoD are the same, because the y-axes of the transmitter and the receiver are the same. Second, for the single-reflected rays, the AoA and the AoD are either the same when the reflection is on the left or the right wall, or supplementary angles (i.e., adding up to 180°) when the reflection is on the front or the back wall. Third, for the twice-reflected ray that reflects on the right and then left surfaces, the AoD is 0° while the AoA is 180°. Lastly, for the scattered rays, the AoDs and the AoAs are not strictly coupled due to the angle scattering effects.

To evaluate the spread of the elevation angle profile, the rms angular spread can be obtained in a similar fashion as the rms delay spread, by replacing the delay τ in (22) and (23) with the angle θ [22]. The resulting rms angular spread in the elevation plane is 0.12^{o}, which is $1/10$ of the rms angular spread in the omni-directional antenna case. The elevation angular spread varies and has some dependency on the heights of the transmitter and the receiver, the communication distance and the propagation environment. In general, the elevation angular spread increases when the height difference between the transmitter and the receiver reduces, and when the communication distance decreases. On the other hand, the azimuth AoD and AoA are demonstrated in Fig. 5(b). Different from the elevation PAP, the range of the azimuth angles extends to -180^{o} and 180^{o}. The zero degree points to the positive x-axis, and the degree increases clockwisely, towards the positive y-axis. The azimuth rms angular spread is 1.3^{o}. Although the rays propagate in a large range of azimuth angles, the rms angular spread in the azimuth plane is small, due to the beamforming effect by using the reflectarray antenna.

D. Wideband Channel Capacity

The wideband capacity in the 3-D end-to-end model in the THz band can be calculated as

$$C = \sum_{n=1}^{N} \Delta f \log(1 + \frac{|H_{\text{e2e}}(f_n)|^2 P_n}{\Delta f W_N}), \tag{24}$$

where N refers to the total number of sub-bands for the transmission, $\Delta f = 1$ GHz is the width of each sub-band that is smaller than the coherence bandwidth found in Sec. V-B, to ensure narrowband communications. P_n denotes the transmit power in the n^{th} sub-band and the total transmit power $\sum_{n=1}^{N} P_n$ is fixed. H_{e2e} is the transfer function as given in (1), and $W_N = -85$ dBm/GHz stands for power spectral density of the additive white Gaussian noise. Since the graphene-based antenna can support wideband transmissions, whose bandwidth can reach up to 15% of the carrier frequency [19], a bandwidth of 100 GHz is considered to compute the capacity.

The wideband channel capacities under the water-filling (WF) and equal-power (EP) allocation schemes are numerically evaluated, for the different transmit power levels at the distance $d = 5$m. The WF allocation scheme has one higher order of magnitude of capacity than the EP scheme in general. In Fig. 6(a), the 18-dB-gain graphene-based reflectarray antenna is used at the transmitter. The capacities for the three different bands, namely, (0.3-0.4) THz, (0.6-0.7) THz, and (0.9-1) THz are compared. Due to the degradation of the path gain, the channel capacity decreases as the frequency increases. In particular, the capacity over (0.3-0.4) THz is nearly ten times higher than that over (0.9-1) THz.

This article has been accepted for publication in a future issue of this journal, but has not been fully edited. Content may change prior to final publication. Citation information: DOI 10.1109/TVT.2016.2614335, IEEE Transactions on Vehicular Technology

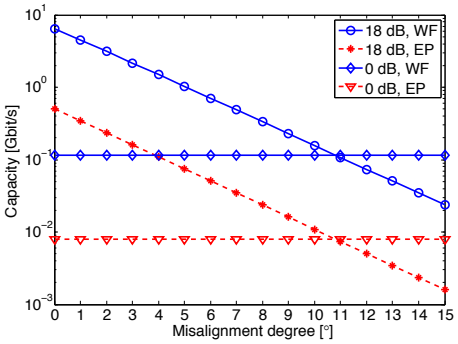

Fig. 7. Channel capacity with the beam misalignment. The transmit power is 10 dBm, the frequency band is (0.9-1) THz, and the distance is 5m.

In Fig. 6(b), the use of the entire (0.06-1) THz band and the utilization of 100 GHz bandwidth are compared. Even with the use of the reflectarray antenna, 100 Gbps rate is not achievable over (0.3-0.4) THz. On the contrary, 100 Gbps can be obtained when the (0.06-1) THz band is simultaneously explored, for the transmit power above 4 dBm under the WF scheme. Furthermore, the capacity over the (0.3-0.4) THz band with the WF scheme is even worse than that over the (0.06-1) THz band with the EP scheme. This shows the substantial advantage of the large bandwidth even when the transmit power is unchanged. Fig. 6(c) demonstrates the merit of the reflectarray antenna over the omni-directional antenna at the transmitter. With the same transmit power and the same allocation scheme, the capacity is improved by almost one hundred times thanks to the 18 dB reflectarray antenna gain. In the (0.9-1) THz band, 0.1 Gbits/s is achievable when the transmit power is 10 dBm under the WF scheme when there is no transmit antenna gain. By contrast, 6.47 Gbps can be obtained when the reflectarray gain is applied, given the same transmit power and the same allocation scheme. This comparison suggests the significance of the antenna gain for enabling ultra-high-speed communications in the THz band.

E. Beam Misalignment

In reality, perfect antenna alignment cannot be achieved, and the beam misalignment would degrade the channel performance. To study the effect of the beam misalignment, we assess the channel capacity using (24) for the (0.9-1) THz band with the different antenna gains and the varying levels of misalignment, as illustrated in Fig. 7. The misalignment level is defined as the angle between the actual main beam direction and the perfect alignment direction in the azimuth plane, while the misalignment in the elevation is negligible owing to the very small elevation angular spread, as found in Sec. V-C. The transmit power is 10 dBm under the WF and EP allocation schemes, and the distance is 5m.

When the alignment is perfect, the channel capacity is equivalent to the results in Sec. V-D. As the misalignment angle increases from 0^o to 15^o, the WF channel capacity decreases considerably, from 6.47 Gbps to 23.5 Mbps. This is due to the substantial reduction of the beamforming gain in the reflectarray antenna. The result agrees with the gain and beamwidth analysis in Sec. V-A. In comparison, the channel capacity in the isotropic antenna case keeps at 0.12 Gbps regardless of the increase of the misalignment degree, since the antenna gain is uniform in the 3-D environment. Interestingly, the capacity performance with the reflectarray antenna becomes worse than the omni-directional antenna case when the misalignment angle is larger than 11°. Therefore, the reflectarray brings the beamforming gain, which is significant for enabling ultra-high-speed communications in the THz band. However, the gain is at the cost of a strict beam alignment requirement. Indeed, the requirement for alignment becomes stricter if the beamforming is adopted at both the transmitter and the receiver. The compromise between the directivity gain and the misalignment tolerance is an important factor that needs to be accounted for in the system design.

F. Differences between 3-D and 2-D Channel Characteristics

By analyzing the EM wave propagation from the transmit antenna to the receive antenna in the 3-D environment, the channel characteristics are found to be different from our prior 2-D multi-path channel model [10], and are summarized as follows. First, additional multi-path rays arrive at the receiver as the elevation plane is incorporated in addition to the azimuth plane. This results in a higher delay spread and a small coherence bandwidth. Second, the angular spread particularly in the elevation plane opens up new opportunities for exploring the diversity gain and also enabling massive MIMO communications with sufficient spatial degrees of freedom. Third, with the use of the graphene-based reflectarray antenna, a 18 dB gain can be achieved in the main beam. This gain improves the channel capacity substantially and equivalently, the communication distance could be enhanced. Fourth, the beamforming gain imposes challenges on the end-to-end link design in terms of the strict 3-D beam alignment requirement.

VI. Conclusion

In this paper, we have developed a generic channel model that includes the graphene-based reflectarray antenna response and the 3-D multi-path propagation phenomena. Related to vehicular networks, the proposed model can be applied in intelligent transport systems for intra-vehicle, inter-vehicle and vehicle-to-roadside wireless ultra-broadband links. In particular, we have investigated the architecture of a graphene-based reflectarray antenna and modeled the 3-D radiation pattern. Moreover, we developed the 3-D multi-path channel model based on ray tracing techniques.

By using the developed model, we have presented an in-depth analysis on the 3-D channel characteristics. First, the gain at the main beam of the graphene-based reflectarray antenna is 18 dB, and the 3-dB beamwidths in the elevation and azimuth planes are 7^o and 10^o respectively. Second, the use of the reflectarray leads to the decrease of the delay spread from 1.23 ns to 0.099 ns, and the resulting coherence bandwidth reaches 2 GHz. Third, the rms angular spread in the elevation plane is less than 0.12^o, which is 1/10 of that without beamforming. Fourth, we analyzed the wideband capacity of the 3-D channel, which can be enhanced with a larger transmit

power, a smaller operating frequency band, a larger bandwidth and a higher beamforming gain. Finally, the beamforming gain enabled by the reflectarray antenna is compromised at the cost of the strict beam alignment, and the deviation needs to be smaller than 11°. The provided analysis and the channel physical parameters lay out the foundation, and are particularly useful for the physical and upper layers design of reliable and efficient ultra-high-speed THz wireless communications.

REFERENCES

[1] T. Kleine-Ostmann and T. Nagatsuma, "A Review on Terahertz Communications Research," *Journal of Infrared, Millimeter and Terahertz Waves*, vol. 32, pp. 143–171, 2011.

[2] H. Song and T. Nagatsuma, "Present and Future of Terahertz Communications," *IEEE Transactions on Terahertz Science and Technology*, vol. 1, no. 1, pp. 256–263, 2011.

[3] I. F. Akyildiz, J. M. Jornet, and C. Han, "TeraNets: Ultra-broadband Communication Networks in the Terahertz Band," *IEEE Wireless Communications Magazine*, vol. 21, no. 4, pp. 130–135, 2014.

[4] ——, "Terahertz Band: Next Frontier for Wireless Communications," *Physical Communication (Elsevier) Journal*, vol. 12, pp. 16–32, 2014.

[5] P. Papadimitratos, A. La Fortelle, K. Evenssen, R. Brignolo, and S. Cosenza, "Vehicular communication systems: Enabling technologies, applications, and future outlook on intelligent transportation," *IEEE Communications Magazine*, vol. 47, no. 11, pp. 84–95, 2009.

[6] T. Aulin, "A modified model for the fading signal at a mobile radio channel," *IEEE Transactions on Vehicular Technology*, vol. 28, no. 3, pp. 182–203, 1979.

[7] S. Qu and T. Yeap, "A three-dimensional scattering model for fading channels in land mobile environment," *IEEE Transactions on Vehicular Technology*, vol. 48, no. 3, pp. 765–781, 1999.

[8] Y. Z. Mohasseb and M. P. Fitz, "A 3-D spatio-temporal simulation model for wireless channels," *IEEE Journal on Selected Areas in Communications*, vol. 20, no. 6, pp. 1193–1203, 2002.

[9] J. M. Jornet, and I. F. Akyildiz, "Channel Modeling and Capacity Analysis for Electromagnetic Wireless Nanonetworks in the Terahertz Band," *IEEE Transactions on Wireless Communications*, vol. 10, no. 10, pp. 3211–3221, 2011.

[10] C. Han, A. O. Bicen, and I. F. Akyildiz, "Multi-Ray Channel Modeling and Wideband Characterization for Wireless Communications in the Terahertz Band," *IEEE Transactions on Wireless Communications*, vol. 14, no. 5, pp. 2402–2412, 2015.

[11] S. Priebe, M. Kannicht, M. Jacob, and T. Kurner, "Ultra-broadband indoor channel measurements and calibrated ray tracing propagation modeling at THz frequencies," *IEEE Journal of Communications and Networks*, vol. 15, no. 6, pp. 547–558, 2013.

[12] K. Yasuko and S. Takamasa, "Terahertz-wave Propagation Model," *Journal of the National Institute of Information and Communications Technology*, vol. 55, no. 1, pp. 73–77, 2008.

[13] M. Dragoman, A. Muller, D. Dragoman, F. Coccetti, and R. Plana, "Terahertz antenna based on graphene," *Journal of Applied Physics*, vol. 107, no. 10, p. 104313, 2010.

[14] M. Tamagnone, J. Gomez-Diaz, J. Mosig, and J. Perruisseau-Carrier, "Analysis and design of Terahertz antennas based on plasmonic resonant graphene sheets," *Journal of Applied Physics*, vol. 112, no. 11, p. 114915, 2012.

[15] J. M. Jornet and I. F. Akyildiz, "Graphene-based Plasmonic Nano-antenna for Terahertz Band Communication in Nanonetworks," *IEEE JSAC, Special Issue on Emerging Technologies for Communications*, vol. 31, no. 12, pp. 685–694, 2013.

[16] J. Huang, *Reflectarray Antenna*. Wiley Online Library, 2005.

[17] W. Menzel, D. Pilz, and M. Al-Tikriti, "Millimeter-wave folded reflector antennas with high gain, low loss, and low profile," *IEEE Antennas and Propagation Magazine*, vol. 44, no. 3, pp. 24–29, 2002.

[18] T. Niu, W. Withayachumnankul, B. S.-Y. Ung, H. Menekse, M. Bhaskaran, S. Sriram, and C. Fumeaux, "Experimental demonstration of reflectarray antennas at Terahertz frequencies," *Optics express*, vol. 21, no. 3, pp. 2875–2889, 2013.

[19] E. Carrasco and J. Perruisseau-Carrier, "Reflectarray antenna at Terahertz using graphene," *IEEE Antennas and Wireless Propagation Letters*, vol. 12, pp. 253–256, 2013.

[20] P. Nayeri, M. Liang, R. A. Sabory-Garcia, M. Tuo, F. Yang, M. Gehm, H. Xin, and A. Z. Elsherbeni, "3D printed dielectric reflectarrays: low-cost high-gain antennas at sub-millimeter waves," *IEEE Transactions on Antennas and Propagation*, vol. 62, no. 4, pp. 2000–2008, 2014.

[21] J. M. Jornet and I. F. Akyildiz, "Femtosecond-Long Pulse-Based Modulation for Terahertz Band Communication in Nanonetworks," *IEEE Transactions on Communications*, vol. 62, no. 5, pp. 1742–1754, 2014.

[22] C. Zhang, C. Han, and I. F. Akyildiz, "Three Dimensional End-to-end Modeling and Directivity Analysis for Graphene-based Antennas in the Terahertz Band," in *Proc. of IEEE Globecom*, 2015.

[23] E. Torkildson, U. Madhow, and M. Rodwell, "Indoor millimeter wave MIMO: Feasibility and performance," *IEEE Transactions on Wireless Communications*, vol. 10, no. 12, pp. 4150–4160, 2011.

[24] B. Sensale-Rodriguez, R. Yan, L. Liu, D. Jena, and H. G. Xing, "Graphene for reconfigurable Terahertz optoelectronics," *Proceedings of the IEEE*, vol. 101, no. 7, pp. 1705–1716, 2013.

[25] J. M. Dawlaty, S. Shivaraman, J. Strait, P. George, M. Chandrashekhar, F. Rana, M. G. Spencer, D. Veksler, and Y. Chen, "Measurement of the optical absorption spectra of epitaxial graphene from Terahertz to visible," *Applied Physics Letters*, vol. 93, no. 13, p. 131905, 2008.

[26] M. Jacob, S. Priebe, R. Dickhoff, T. Kleine-Ostmann, T. Schrader, and T. Kürner, "Diffraction in mm and sub-mm Wave Indoor Propagation Channels," *IEEE Transactions on Microwave Theory and Techniques*, vol. 60, no. 3, pp. 833–844, 2012.

[27] R. Piesiewicz, C. Jansen, D. Mittleman, T. Kleine-Ostmann, M. Koch, and T. Kurner, "Scattering Analysis for the Modeling of Terahertz Communication Systems," *IEEE Transactions on Antennas and Propagation*, vol. 55, no. 11, pp. 3002–3009, Nov. 2007.

[28] E. Carrasco, M. Tamagnone, and J. Perruisseau-Carrier, "Tunable graphene reflective cells for THz reflectarrays and generalized law of reflection," *Applied Physics Letters*, vol. 102, no. 10, p. 104103, 2013.

Chong Han (M'16) received the Bachelor of Engineering degree in Electrical Engineering and Telecommunications from The University of New South Wales, Sydney, Australia, in 2011. He obtained the Master of Science and the Ph.D. degrees in Electrical and Computer Engineering from Georgia Institute of Technology, Atlanta, GA, USA, in 2012 and 2016, respectively. He is currently an Assistant Professor and Associate Special Research Fellow with the University of Michigan–Shanghai Jiao Tong University Joint Institute, Shanghai Jiao Tong University, Shanghai 200240, China. His current research interests include Terahertz band communication networks, 5G cellular networks, Electromagnetic nanonetworks, Graphene-enabled wireless communications.

Ian F. Akyildiz (M'86-SM'89-F'96) received the B.S., M.S., and Ph.D. degrees in Computer Engineering from the University of Erlangen-Nurnberg, Germany, in 1978, 1981 and 1984, respectively. Currently, he is the Ken Byers Chair Professor in Telecommunications with the School of Electrical and Computer Engineering, Georgia Institute of Technology, Atlanta, the Director of the Broadband Wireless Networking Laboratory and Chair of the Telecommunication Group at Georgia Tech. Dr. Akyildiz is an honorary professor with the School of Electrical Engineering at Universitat Politecnica de Catalunya (UPC) in Barcelona, Catalunya, Spain and founded the N3Cat (NaNoNetworking Center in Catalunya). Since September 2012, Dr. Akyildiz is also a FiDiPro Professor (Finland Distinguished Professor Program (FiDiPro) supported by the Academy of Finland) at Tampere University of Technology, Department of Communications Engineering, Finland. He is the Editor-in-Chief of Computer Networks (Elsevier) Journal, and the founding Editor-in-Chief of the Ad Hoc Networks (Elsevier) Journal, the Physical Communication (Elsevier) Journal and the Nano Communication Networks (Elsevier) Journal. He is an IEEE Fellow (1996) and an ACM Fellow (1997). He received numerous awards from IEEE and ACM. His current research interests are in Terahertz band communication, nanonetworks, software defined networking, 5G cellular systems and wireless underground sensor networks.